Geometry and dynamics link form, function, and evolution of finch beaks

Salem al-Mosleh[a], Gary P. T. Choi[a,b], Arhat Abzhanov[c,d], and L. Mahadevan[a,e,f,1]

[a]John A. Paulson School of Engineering and Applied Sciences, Harvard University, Cambridge, MA 02138; [b]Department of Mathematics, Massachusetts Institute of Technology, Cambridge, MA 02139; [c]Department of Life Sciences, Imperial College London, Ascot SL5 7PY, United Kingdom; [d]Department of Life Sciences, Natural History Museum, London SW7 5BD, United Kingdom; [e]Department of Organismic and Evolutionary Biology, Harvard University, Cambridge, MA 02138; and [f]Department of Physics, Harvard University, Cambridge, MA 02138

Edited by Neil H. Shubin, University of Chicago, Chicago, IL, and approved August 11, 2021 (received for review March 28, 2021)

Darwin's finches are a classic example of adaptive radiation, exemplified by their adaptive and functional beak morphologies. To quantify their form, we carry out a morphometric analysis of the three-dimensional beak shapes of all of Darwin's finches and find that they can be fit by a transverse parabolic shape with a curvature that increases linearly from the base toward the tip of the beak. The morphological variation of beak orientation, aspect ratios, and curvatures allows us to quantify beak function in terms of the elementary theory of machines, consistent with the dietary variations across finches. Finally, to explain the origin of the evolutionary morphometry and the developmental morphogenesis of the finch beak, we propose an experimentally motivated growth law at the cellular level that simplifies to a variant of curvature-driven flow at the tissue level and captures the range of observed beak shapes in terms of a simple morphospace. Altogether, our study illuminates how a minimal combination of geometry and dynamics allows for functional form to develop and evolve.

beaks | morphology | Darwin's finches | evo–devo

Darwin's finches, a family of 14 to 16 bird species (Fig. 1) that likely evolved from a common ancestor arriving in the Galàpagos 2 to 3 Ma, form a classic example of adaptive radiation (1). This group has an extremely high diversification rate when compared with other birds including related species on the mainland and all other avian inhabitants of Galàpagos (2). The evolutionary and ecological success of Darwin's finches is closely associated with the disparity and diversity of beak morphology (3, 4), ranging from the broad, blunt beak of the large ground finch *Geospiza magnirostris* to the thin and pointed beak of the warbler finch *Certhidea olivacea* (5). Each species of Darwin's finches has a unique beak shape, which affords them distinct strategies for both exploration and exploitation of different types of diets (e.g., *G. magnirostris*: seeds; *C. olivacea*: insects) (Fig. 1*A*). This morphological diversity is generated by modifications to an otherwise conserved beak developmental program (6–9). To fully explain the observed diversity of beak shapes in Darwin's finches and other birds, we need to integrate perspectives from evolutionary biology and developmental genetics with mathematical morphometry, the biophysics of morphogenesis, and the biomechanics of beak function, unifying the study of growth, form, and function.

Here, we quantify the diversity of all finch beaks using three-dimensional (3D) morphometry (10, 11). This leads to a minimal morphospace that allows us to quantify the beak's mechanical function as a machine (12–14) and show how beak angle relative to the skull, aspect ratios, and curvatures affect the ability of the bird to apply and withstand biting forces. To explain this evolutionary variation across species along with the observed dynamics of beak development in zebra finches (6, 9, 15), we propose an experimentally motivated simple biophysical law for beak morphogenesis that links growth to surface curvature and yields a morphospace consistent with observations.

Evolutionary Morphospace of Beaks

To quantify the 3D shape of beaks, we used high-resolution 3D computed tomography (CT) scans (16) of the skulls and used a smoothing algorithm (*SI Appendix* has details) to obtain the 3D surface of the upper beak, as shown in Fig. 1*B* (Movie S1), moving away from previous morphological analyses based either on discrete metrics such as length, width, and depth (10, 11) or on two-dimensional approaches (15). In Fig. 1*C*, we show the result of 59 micro-CT (μCT) scans of upper beaks from 15 different species in the genera *Geospiza*, *Camarhynchus*, *Certhidea*, *Pinaroloxias*, *Platyspiza*, and *Tiaris* along with their phylogenetic relationships.

Denoting the origin at the tip of the beak, with axes oriented to correspond to the principal axes of the beak (Fig. 2*A*), we find that the following paraboloidal profile captures the surface of the upper beak (Fig. 2*B* and *SI Appendix*, Figs. S1–S4):

$$z(x,y) = \frac{D + \kappa_x L^2}{L}\, x - \kappa_x\, x^2 - (\kappa_{tip} - S\, x)\; y^2, \qquad [1]$$

where L, W, D are the length, width, and depth, respectively; κ_x is the curvature of the midsagittal section; κ_{tip} is the curvature in the transverse direction at the tip; and S represents the "sharpening rate" of the beak curvature toward the tip. Since the size of the cross-section shrinks to zero at the tip, the parameter κ_{tip} is extracted from the linear fit of the transverse curvature $\kappa_y \equiv \kappa_{tip} - S\, x$. This allows us to represent each beak as a point in a 3D morphospace with coordinates $(\kappa_x, \kappa_{tip}, S)$ as shown in Fig. 2*C*. To compare beak shape across species, we remove the effect of scale and consider the dimensionless shape variables $\tilde{\kappa}_x \equiv \frac{L^2}{D}\,\kappa_x$, $\tilde{\kappa}_{tip} \equiv \frac{W^2}{D}\,\kappa_{tip}$, and $\tilde{S} \equiv \frac{L\,W^2}{D}\,S$ (Eq. **2**). Further noting that the beak is cut by the plane $z = 0$, we have

Significance

Understanding how development and evolution shape functional morphology is a basic question in biology. A paradigm of this is the finch's beak that has adapted to different diets and behaviors over millions of years. We take a mathematical and physical perspective to quantify the nature of beak shape variations, how they emerge from changes to the development program of the birds, and their functional significance as a mechanical tool.

Author contributions: S.a.-M., G.P.T.C., A.A., and L.M. designed research; S.a.-M., G.P.T.C., and L.M. performed research; S.a.-M., G.P.T.C., A.A., and L.M. analyzed data; and S.a.-M. and L.M. wrote the paper.

The authors declare no competing interest.

This article is a PNAS Direct Submission.

[1]To whom correspondence may be addressed. Email: lmahadev@g.harvard.edu.

This article contains supporting information online at https://www.pnas.org/lookup/suppl/doi:10.1073/pnas.2105957118/-/DCSupplemental.

Published November 8, 2021.

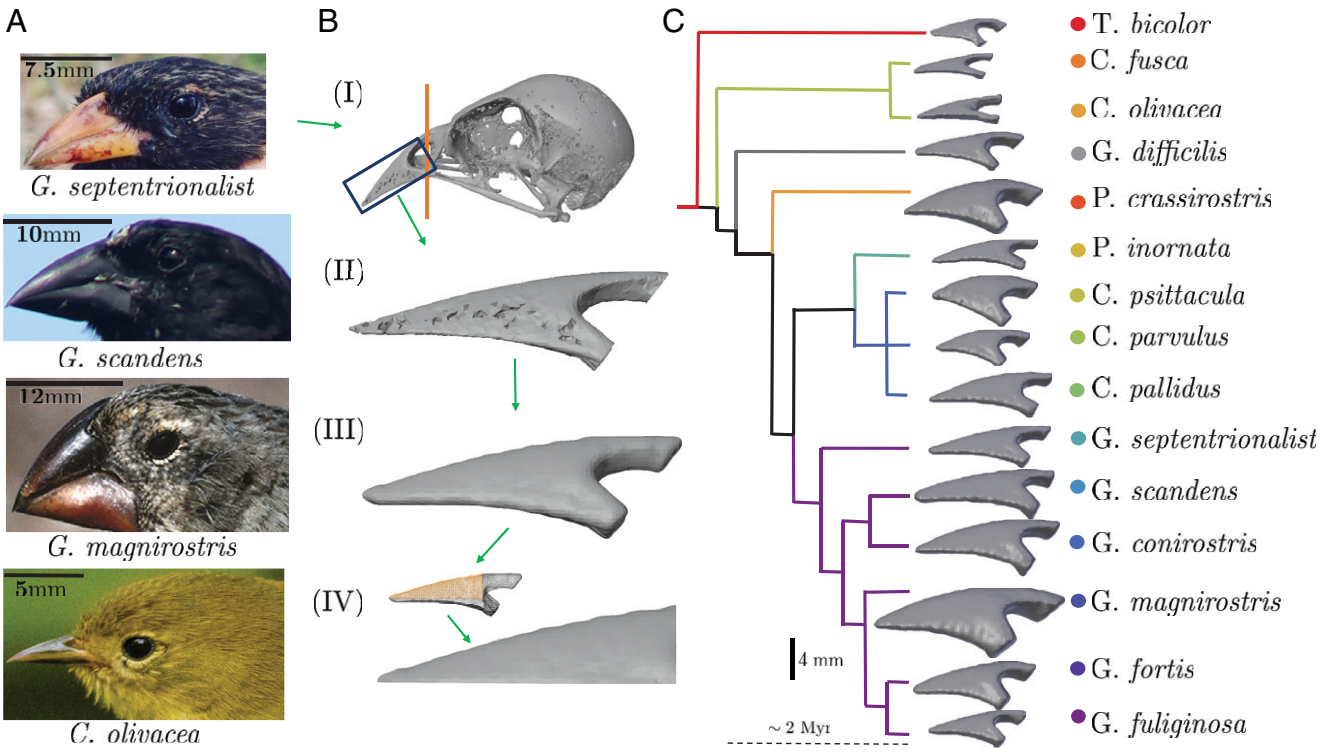

Fig. 1. Beak morphology and phylogeny of Darwin's finches. (*A*) Adaptive radiation of Darwin's finches is reflected in the diversity of beak sizes and shapes associated with specialized diets, including (from top to bottom) drawing blood, drinking nectar, crushing seeds, and catching insects. Image credit (Fig. 1*A*, *from Top to Bottom*): Daniel Baldassarre (State University of New York at Oswego, Oswego, NY); Jamie Krupka (Macaulay Library at the Cornell Lab of Ornithology, Ithaca, NY); Arhat Abzhanov; and Richard Thunen (Macaulay Library at the Cornell Lab of Ornithology, Ithaca, NY). (*B*) Protocols for shape extraction used in the analysis of the beak μCT scans. The orange line in *I* represents the cutting (transverse) plane drawn through the basal end of the beak; the beak is then digitally meshed, and its profile is smoothed (*SI Appendix* has details). *I*: Full "*Geospiza septentrionalist*" skull. *II*: Upper beak cut. *III*: Smoothed upper beak. *IV*: Upper beak surface. (*C*) Molecular phylogeny of Darwin's finches over the past 2 to 3 My (represented by the dashed line). Shown are *Tiaris bicolor*, *Certhidea fusca*, *C. olivacea*, *Geospiza difficilis*, *P. crassirostris*, *Platyspiza inornate*, *C. psittacula*, *Camarhynchus parvulus*, *C. pallidus*, *G. septentrionalist*, *G. scandens*, *Geospiza conirostris*, *G. magnirostris*, *Geospiza fortis*, and *Geospiza fuliginosa*.

the additional relation $z(L, W/2) = 0$, which yields the identity $\tilde{\kappa}_{tip} = 4 + \tilde{S}$ (the Pearson correlation coefficient between the two quantities across our 59 samples is $Cor[\tilde{S}, \tilde{\kappa}_{tip}] \approx 0.995$) (Fig. 2*D*). This reduces the entire morphospace of beak shapes to an overall size $\sqrt{L^2 + W^2 + D^2}$, two aspect ratios associated with the relative depth D/L and width W/L, and two scaled curvature parameters $\tilde{\kappa}_x, \tilde{S}$.

Looking for patterns across beaks after alignment according to their principal directions (PDs), the depth to length ratio is nearly constant across all samples when measured along the PD of the beak but varies by a factor of seven when measured along the PD of the entire skull (*SI Appendix*, Fig. S5). This observation may appear to be in contradiction with the known fact that *G. magnirostris* beaks have larger depth to length ratios compared with *Geospiza scandens*. However, as can be seen in Fig. 1*A*, the different orientations of the beaks relative to the head explain a large part of the apparent variation in aspect ratios.

Form and Mechanical Function of Beaks

While several factors can influence beak shape evolution (17–19), feeding ecology is thought to play a primary role in selection pressure on the beaks of Darwin's finches (20, 21) and other birds (22). Indeed, the morphological patterns of variation (*SI Appendix*, Fig. S6) in beak shape are correlated strongly with beak function as a mechanical tool. For example, beaks of the large tree finch, the large ground finch, and the vegetarian finch have larger curvature and sharpening rate (*SI Appendix*, Fig. S5) and are associated with large biting forces. In particular, the large tree finch has the largest sagittal curvature $\tilde{\kappa}_x$, the large ground finch has the highest sharpening rate $\tilde{S}$, and the vegetarian finch is the second highest on both dimensions. In contrast, insect eating and probing beaks, such as those of warbler and cactus finches, have relatively lower curvature and sharpening rate. Compared with birds with strong bite force, the beak to skull angle is much smaller in this case as well.

In order to quantify the mechanical performance for each specimen in Dataset S1, we use the mechanical advantage $\mathcal{M}$, which gives the ratio of input to output forces. The full mechanical advantage can be expressed as the product of factors coming from the different force-propagating structures (23, 24). Here, we focus on factors affected by beak shape. Specifically, $\mathcal{M}$ is the ratio of the input moment arm $[d_1 \sin(\theta)]$ to the output moment arm $[d_2 \sin(\phi)]$ (25), which is illustrated in Fig. 3*A*. The longer the output lever, which corresponds to a smaller $\mathcal{M}$, the faster the closing speed at the tip for a given rotational velocity at the joint (19, 26) (indicated as the orange triangle in Fig. 3*A*). However, smaller lengths of an output lever result in higher forces at the tip for the same input force. Therefore, we expect $\mathcal{M}$ to be highest among species that rely on tip biting such as *Camarhynchus psittacula* and *Platyspiza crassirostris* (*SI Appendix*, Figs. S7 and S8). Species that rely on strong bite forces, such as *G. magnirostris*, also score high on this measure. On the other hand, insect eaters such as *C. olivacea* that require a faster bite at the tip will score lower on this scale, as will species with probing beaks, such as *G. scandens* and *Camarhynchus pallidus*.

To understand the role that beak shape plays in force generation, we consider a simple mechanical analog of the beak shown

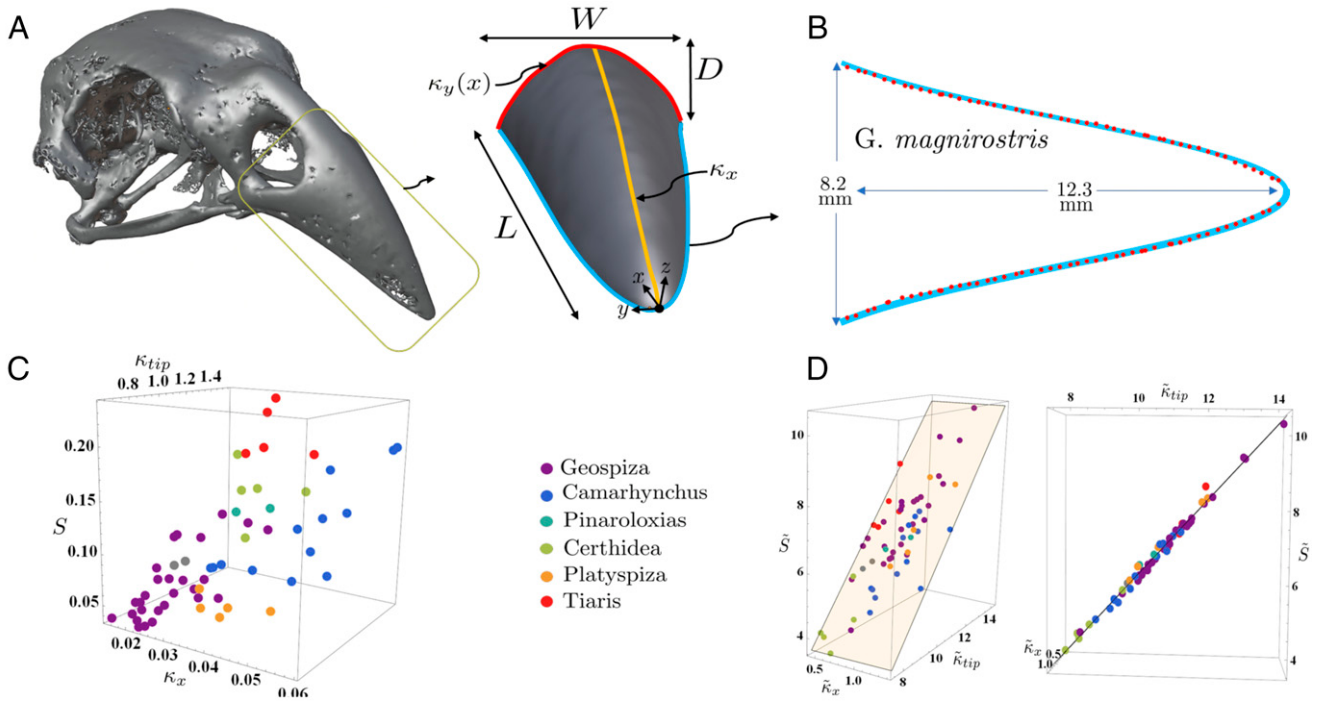

Fig. 2. Evolutionary morphospace of beaks. (*A*) Digitally extracting the upper beak from the skull (*Left*) of *G. septentrionalist* and aligning the result with its PDs (Fig. 1*B*) yield the smoothed shape (*Right*). The midsagittal curve (yellow), $y = 0$, is fit well with a parabolic form, $z = (D + \kappa_x L^2)(x/L) - \kappa_x x^2$. The transverse sections, shown in red, at the basal end can be fit well with parabolas whose curvatures vary linearly with distance from the tip, $\kappa_y(x) = \kappa_{tip} - S x$. Here, $\kappa_{tip} \equiv \kappa_y(0)$. (*B*) The horizontal cross-section $z = 0$ (light blue) as predicted from Eq. **1** agrees well with the actual cut beak (red points). (*C*) The 59 finch beak samples in the morphospace defined by $(\kappa_x, \kappa_{tip}, S)$ in units of (mm^{-1}, mm^{-1}, mm^{-2}) are color coded according to genus. (*D*) Multiple views of the morphospace characterized by the dimensionless parameters $\tilde{\kappa}_x = L^2\,\kappa_x/D$, $\tilde{\kappa}_{tip} = W^2\,\kappa_{tip}/D$, and $\tilde{S} = L\,W^2\,S/D$. The fact that points lie on a plane is confirmation of the parabolic nature of the basal transverse cross-section (*SI Appendix*, Fig. S5).

in Fig. 3*A* (*SI Appendix*, Fig. S9). Here, the blue circles represent the biting point, which in seed-cracking birds, is in the back of the beak as shown in refs. 12 and 14. Using the arrangement shown in the figure, we can calculate the mechanical advantage as a function of the two aspect ratios W/D and D/L. The result, shown in Fig. 3*B*, shows that the mechanical advantage is highly sensitive to D/L and weakly dependent on W/D. The strong D/L dependence is due to the fact that high values of this aspect ratio lead to a decrease in both the angle ϕ and the distance from the joint to the point of force application d_2 (Fig. 3*A*). Indeed, we see that for *G. magnirostris*, $D/L \approx 2$, which is just enough to maximize the value of the mechanical advantage (Fig. 3*C*). The weak dependence of the mechanical advantage on W/D is consistent with the fact that this aspect ratio is nearly constant across all our samples (with the exception of the insect eater *C. olivacea*) (Fig. 3*B*).

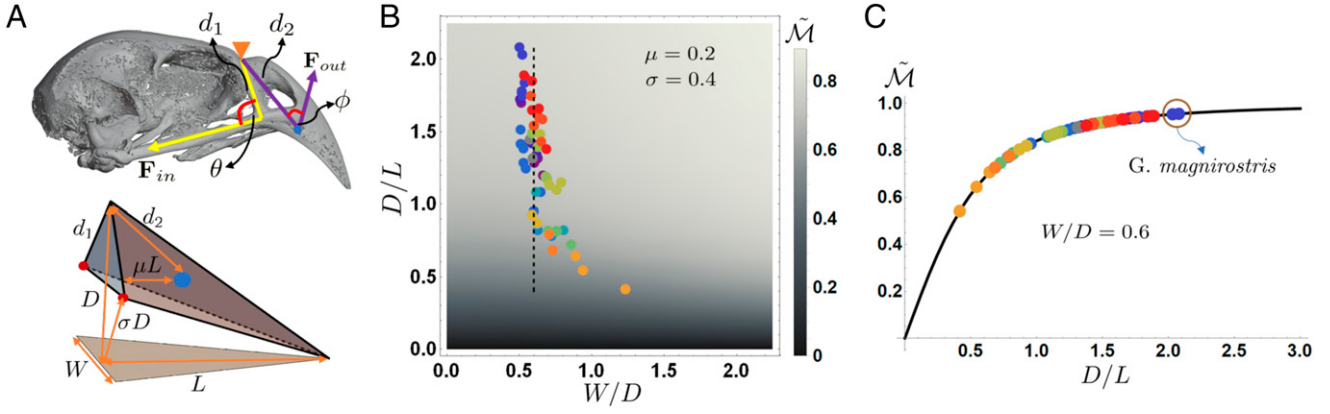

Fig. 3. Functional mechanics of beaks. (*A*) Using a *G. magnirostris* beak sample (*Upper*), we calculate the mechanical advantage of the beak, $\mathcal{M} \equiv |\mathbf{F}_{out}|/|\mathbf{F}_{in}|$, in terms of the input and output forces on the beak (see text). A simplified model of the beak (*Lower*) aids in visualizing the mechanical advantage; the parameter μ characterizes the position of seed placement (blue dot), and σ characterizes the point of application of the input force (red dots). (*B*) The geometric ratios D/L and W/D are color coded as in Fig. 1*C*. The gray scale of the density plot shows the scaled mechanical advantage, $\tilde{\mathcal{M}} \equiv \mathcal{M}/\mathcal{M}_{max}$. As can be seen from the plot, the dependence of $\tilde{\mathcal{M}}$ on W/D is weak. (*C*) The dependence of $\tilde{\mathcal{M}}$ on D/L for $W/D = 0.6$, corresponding to the dashed line in *B*. Note how *G. magnirostris* samples have the highest values of D/L in part due to the large beak angle relative to the skull, thus maximizing their mechanical advantage, $\tilde{\mathcal{M}} \sim 1$.

Additionally, it is well known that stiffness of a mechanical structure can increase with its curvature. In our samples, we see strong correlation between the mechanical advantage, which gives a measure of the forces experienced by the beak and curvature: $Cor[\mathcal{M}, \tilde{\kappa}_{tip} \times \tilde{\kappa}_x] = 0.65$ (*SI Appendix*, Fig. S10). Our mechanical analysis based on the geometry of the beak correlates with the observed morphometry and raises the question of how evolvable these shapes are based on our knowledge of the underlying developmental programs.

Generative Models for Beak Growth and Form

To glean information about the growth patterns that give rise to the range of beak shapes, we consider the developmental dynamics of beak growth and form in the zebra finch (27). Experimentally, beak size and shape are known to depend on the initial orientation of beak growth relative to the skull (28–30). Furthermore, growth occurs only in a primordial group of dividing cells localized near the tip of the developing beak, and the number of dividing cells in the growth zone diminishes over time (9) (Fig. 4*A* and *SI Appendix*, Fig. S11). Then, the initial size, shape, orientation, and dynamics of the extrusion rate of the growth zone along the proximal–distal axis, denoted as U, determine the size and shape of the beak (Fig. 4*B*). Quantifying this can be done using either a cellular model that accounts for cell proliferation and movement patterns in space–time or a coarse-grained tissue-level model for the evolution of the beak treated as a continuum.

Cellular Model for Growth. We start with a minimal cellular model capable of approximating the actual beak cross-sections. We assume that cell proliferation is controlled by the concentration of a morphogen such as FgF or Bmp4, produced by cells in the growth zone, that is approximated by a narrow slice of tissue along the proximal–distal axis. When the concentration of the morphogen at some position drops below a threshold, cells stop dividing there. The morphogen diffuses to the surrounding cells with diffusion constant D_c and degrades at a rate Γ (*Materials and Methods*). This limits the efficacy of the morphogen produced by a cell to a region of size $\lambda \sim \sqrt{D_c/\Gamma}$ (the white circle in Fig. 4*C*). Furthermore, since only cells in the growth zone produce this morphogen, a gradient will be established along the proximal–distal axis from which cells can generate a stable growth in the distal direction.

Through this morphogen, each cell can also sense how far it is from a boundary; cells whose distance from the boundary is smaller than λ will receive morphogen signals from fewer cells (Fig. 4*C*). This naturally implies an effect of the boundary curvature as well; cells proliferate less in more curved regions. A comparison of the shapes generated from this model with parameters fit to match a *C. pallidus* sample is shown in Fig. 4*C*. As the figure shows, such a minimal model is able to recover the shapes generated by beak developmental mechanisms (Movie S2).

Modified Mean Curvature Flow Approximates Beak Development. From the cellular model described above, a simple geometry-driven growth law emerges on the tissue scale (31–34). Intuitively, the shrinkage of the primordial mass of dividing cells suggests a simple geometric rule that the surface of the beak shrinks at a constant rate even as it extrudes distally. Furthermore, since cells near a highly curved part of the boundary have fewer neighbors and therefore, are more likely to stop dividing, the envelope of the growth zone will shrink faster in that region. By looking at transverse sections of the adult beaks (*SI Appendix*, Fig. S13 and Table S1), we observe that regions of higher curvature, which correspond to the midsagittal section ($y = 0$) in Eq. **1**, do in fact shrink faster as one moves closer toward the tip. The combination of experimental observations of the developing finch beak, the range of beak morphologies, and our cellular model suggests that the boundary of the growth zone evolves with a velocity that depends on the local (arc) curvature through the relation $\mathbf{v} = -(a + b\kappa)\mathbf{n}$ in the direction of the inward normal to the surface ($a, b > 0$) (*SI Appendix* has more details). The ratio b/a gives a length scale that

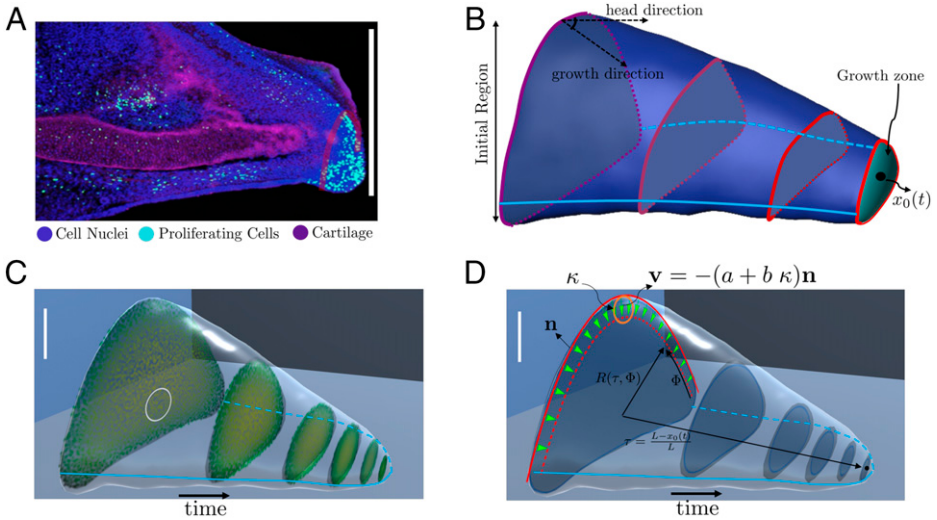

Fig. 4. Growth and form of beaks. (*A*) The active growth zone in a developing beak of a zebra finch at stage 37 (following ref. 7 which shows proliferating cells that are involved in division and growth close to the tip). The red curve delineates the most recent cross-section to exit the growth zone. (*B*) The function $x_0(t)$ is the center of the growth zone at time t. The blue mesh is taken from a *C. pallidus* sample, and the green–blue region near the tip represents the growth zone. Also illustrated is the angle of growth relative to the skull. The red curves represent cross-sections at different times, with more recent ones being brighter. (*C*) Results from the combined boundary and bulk stoppage of cell proliferation model described in the text superimposed with the actual cross-sections from a *C. pallidus* sample. The white circle represents the range, λ, of the morphogen. The initial conditions were generated from a basal cross-section of the actual beak (see *SI Appendix*, Fig. S12 for parameters). (*D*) Results for the same *C. pallidus* sample as above with cross-sections generated from a simulation using the mean curvature flow with $U \equiv dx_0(t)/dt$, $a/U = 0.74$, and $b/U = 2$ mm and the same initial basal cross-section as in *C* (see *SI Appendix*, Fig. S13 and *SI Text* for parameters). The green arrows give the velocity field of the mean curvature flow given by $\mathbf{v} = -(a + b\,\kappa)\mathbf{n}$, where κ is the boundary curvature and $\mathbf{n}$ is the unit normal to the boundary. Also illustrated is a growth-adapted coordinate frame $[\tau, \Phi, R(\tau, \Phi)]$, an alternative parametrization to the Cartesian frame of Eq. **1**. (Scale bars, 1mm.)

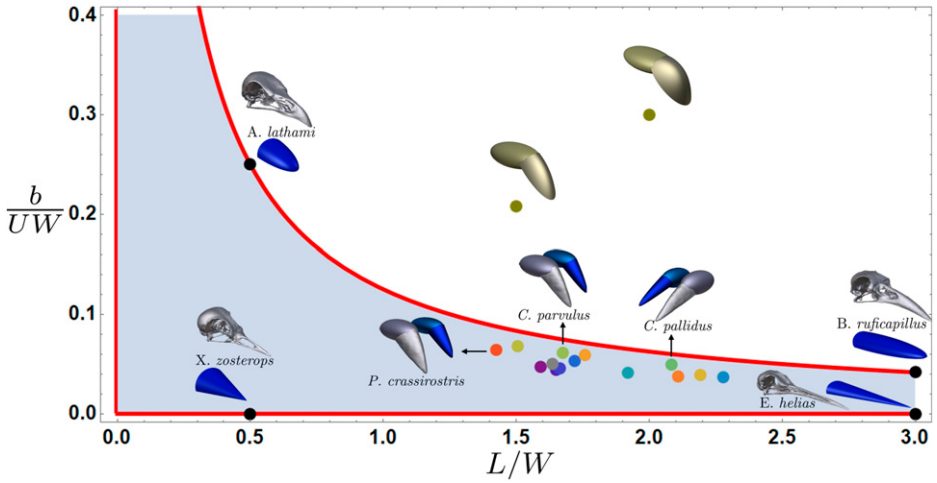

Fig. 5. Developmental morphospace of beaks. Beak shapes were generated using the modified mean curvature flow $\mathbf{v} = -(a + b\kappa)\mathbf{n}$ acting on circular cross-sections with initial radius $R(0) = W/2$. Each point in the phase space corresponds to a species (color coded as in Fig. 1*C*). The parameter a/U is numerically solved for in terms of L/W and $b/(UW)$ to generate the points shown (parameter values are given in *SI Appendix*, Table S2). The light blue region is the region allowed by the mean curvature flow. Note how the points lie inside the region and close to the curve $b/U = W^2/8L$, which corresponds to $a = 0$ (see text for an explanation of this developmental constraint). The four skulls, taken from ref. 39, illustrate the range of shapes generated by this growth law. We also show a few golden-colored beaks with shapes not allowed by the constraint ($L/W = 1.5$, $b/U = 0.21W$, $a/U = -0.34$, $\tilde{S} = 0$, $\tilde{\kappa} = 1.5$ and $L/W = 2$, $b/U = 0.3W$, $a/U = -0.57$, $\tilde{S} = 1$, $\tilde{\kappa} = 5$). *Alectura (A.) lathami; Baryphthengus (B.) ruficapillus; Eurypyga (E.) helias; Xanthomixis (X.) zosterops.*

determines which of the two terms in the growth law will dominate (*SI Appendix*, Table S2). When the radius of curvature κ^{-1} of the transverse beak cross-section is greater than b/a, the term $a\mathbf{n}$, which also describes the evolution of a wave front under Huygens' principle, dominates. When $\kappa^{-1} \ll b/a$, the term $b\kappa$ dominates. This growth law is the well-known curve shortening (or mean curvature) flow in which speed is proportional to the curvature, introduced to account for the erosion of pebbles (35) and grain growth from a melt (36), and has since been the object of much mathematical work (37, 38).

Fig. 4*D* shows the agreement between the shape generated by the mean curvature flow and the cross-sections of a *C. pallidus* sample (*SI Appendix*, Fig. S13). We further validate the mean curvature flow by considering the evolution of semicircular cross-sections and comparing them with the actual upper beaks (Movie S3). The flow equations simplify to an ordinary differential equation for the radius $R(t)$ as a function of time given by $\dot{R}(t) = -(a + b/R(t))$; $R(0) = W/2$. The parameters a and b can be estimated by comparing with the functional form of the beak width near $x \to L$ (Eq. **4** and Fig. 2*B*). The resulting phase space is shown in Fig. 5 (*SI Appendix*, Fig. S14) where each point represents a species, color coded as in Fig. 1. The fact that all the points, obtained independently from morphological parameters (Eq. **10**), lie below the boundary of the region allowed by the morphogenetic model is significant and implies a developmental bias, or constraint, that restricts possible beak morphologies (40). The constraint $b/U < W^2/8L$, which can be rewritten as $4\tilde{\kappa}_x \leq \tilde{S}$, may be understood intuitively since large values of $b > 0$ will lead necessarily to smaller lengths. Thus, there are morphologies (those having large sagittal curvature $\tilde{\kappa}_x$ and small sharpening rate $\tilde{S}$) inaccessible to evolution through variation of this developmental program. As indicated by the proximity of the points in Fig. 5 to the curve $b/(UW) = W/8L$, beaks excluded by the developmental constraint may have adaptive value. For example, larger values of $\tilde{\kappa}_x$ in our mechanical models lead to both higher tip biting force and increased rigidity of the beak.

Conclusion

Our morphometric analysis provides an the understanding of the 3D beak shape using simple interpretable parameters. In addition to beak size, beak shape is determined using its orientation relative to the skull, aspect ratios, and curvatures (Fig. 2). We uncovered, through our morphometric analysis in the context of beak diet and biomechanics, ways in which beak morphology can significantly affect mechanical performance (Fig. 3). This understanding allowed for the construction of tissue- and cell-level growth models that reproduce the observed variety of beak shapes (Fig. 4) and explain features of the distribution of beaks in morphospace (Fig. 5). In particular, our developmental models explain how beak shape emerges due to initial size, growth direction relative to the skull, the distal protrusion velocity of the growth zone, and the transverse shrinkage rate determined by both a and b parameters. While we have focused on Darwin's finches, these parameters can determine the generation of beaks from many different bird groups. How these developmental changes actually occurred over time will remain shrouded by the fog of time, but our hope is that our analysis linking form, function, and evolution in the context of Darwin's finches might serve as a fillip for other similar ventures that might help gradually illuminate these mysteries.

Materials and Methods

Nondimensionalized Form of the Beak. Since we are interested in the differences in shape in addition to differences in size, we construct dimensionless quantities by considering the alternative form of Eq. **1** given as

$$z(x,y) = D\left[(1+\tilde{\kappa}_x)\frac{x}{L} - \tilde{\kappa}_x\left(\frac{x}{L}\right)^2 - \left(\tilde{\kappa}_{tip} - \tilde{S}\frac{x}{L}\right)\left(\frac{y}{W}\right)^2\right]$$
$$\Longrightarrow \tilde{\kappa}_x = \frac{L^2}{D}\kappa_x,\ \tilde{\kappa}_{tip} = \frac{W^2}{D}\kappa_{tip},\ \tilde{S} = \frac{L\,W^2}{D}S. \qquad [2]$$

In deriving this form, we have used the fact that $z(L,0) = D$. Since the beak was cut by a horizontal plane, which we take to be the plane $z = 0$, we also have an additional relation, $z(L, W/2) = 0$. This last constraint gives the relation $\tilde{\kappa}_{tip} = 4 + \tilde{S}$ (Fig. 2*D*).

We can further test Eq. **2** by using $z(x, \pm W(x)/2) = 0$ and $D(x) = z(x,0)$ to find

$$D(\tau) = D\left[(1-\tau)(1+\tilde{\kappa}_x) - \tilde{\kappa}_x(1-\tau)^2\right], \qquad [3]$$

$$W(\tau) = W\sqrt{\frac{4(1-\tau)(1+\tilde{\kappa}_x) - 4\,\tilde{\kappa}_x\,(1-\tau)^2}{4+\tilde{S}\,\tau}}. \qquad [4]$$

The form for $W(\tau)$ is derived using the relation that $\kappa_y(x) = \kappa_{tip} - S\,x = 4D(x)/W^2(x)$ and τ, defined as $\tau \equiv \frac{L-x}{L}$, is zero at the base and equal to one at the tip (Fig. 2*B*). Note that $D(0) \equiv D$ and $W(0) \equiv W$ are the corresponding values at the base of the beak.

The dimensions, measured in millimeters, are in the range $4.3 < L < 12.4$, $2.46 < W < 8.34$, and $0.99 < D < 3.47$. The constant midsagittal curvature, in units of millimeters^{-1}, lies in the range $0.015 < \kappa_x < 0.06$ across all species, while the sharpening rate satisfies $0.036 < S < 0.237$ (millimeters^{-2}), and the curvature at the tip (millimeters^{-1}) lies in the range $0.63 < \kappa_{tip} < 1.55$. For the dimensionless quantities, we obtain $0.41 < \tilde{\kappa}_x < 1.4$, $7.5 < \tilde{\kappa}_{tip} < 14.2$, and $3.7 < \tilde{S} < 10.4$.

The shape of the beak can be reparametrized using a developmentally motivated coordinate frame. Using morphogen gradients, cells can in principle determine how far they are from the growth zone center of mass and boundary (Eq. **7**). Therefore, we parameterize the shape for a cross-section at τ as $R(\tau, \Phi)$ where τ, Φ, and R are illustrated in Fig. 4*D* and $R(\tau, \Phi)$ is given in *SI Appendix*, Eq. S23.

Cellular and Tissue Model. We assume that each cell produces the morphogen χ at a constant rate P, which subsequently diffuses with diffusion constant D_c and degrades at a rate given by Γ. Thus, the concentration of the morphogen $\chi(\mathbf{r}, t)$ obeys the equation

$$\partial_t \chi(\mathbf{r}, t) = D_c\, \nabla^2 \chi(\mathbf{r}, t) - \Gamma\, \chi(\mathbf{r}, t) + P. \qquad [5]$$

We see that there is a characteristic length scale controlled by the balance between diffusion and degradation given by $\lambda \equiv \sqrt{D_c/\Gamma}$. Defining the dimensionless quantities $\tilde{t} \equiv \Gamma\, t$, $\rho \equiv \mathbf{r}/\lambda$, and $\psi \equiv \chi/\chi_0$, where $\chi_0 \equiv P/\Gamma$, we can write Eq. **5** in the following dimensionless form:

$$\partial_{\tilde{t}} \psi(\boldsymbol{\rho}, \tilde{t}) = \nabla^2 \psi(\boldsymbol{\rho}, \tilde{t}) - \psi(\boldsymbol{\rho}, \tilde{t}) + 1,$$
$$\lim_{|\boldsymbol{\rho}| \to \infty} \psi(\boldsymbol{\rho}, \tilde{t}) = 0 \quad \text{and} \quad \psi(\boldsymbol{\rho}, 0) = \psi_{init}(\boldsymbol{\rho}). \qquad [6]$$

If the cell division rate is much smaller than Γ^{-1}, then the concentration of χ will reach a steady state given by

$$\psi(\boldsymbol{\rho}, \tilde{t} \to \infty) = \int_{\mathcal{R}} \frac{e^{-|\boldsymbol{\rho} - \boldsymbol{\rho}'|}}{4\pi |\boldsymbol{\rho} - \boldsymbol{\rho}'|}\, d^3\boldsymbol{\rho}', \qquad [7]$$

where $\mathcal{R}$ is the region containing the morphogen-producing cells. Since the morphogen is only produced in the growth zone, which is located distally, the concentration will decrease exponentially away from this zone. This establishes a morphogen gradient that allows cells to maintain a stable growth direction. Furthermore, the concentration of the morphogen will be maximal in the center of the growth zone since a cell at that location gets contributions from other cells in all directions. We denote this maximal concentration as ψ_{bulk}. Near the boundary, a distance $\epsilon\lambda$ away, a cell has fewer neighbors and experiences lower concentrations as a consequence (*SI Appendix*, Fig. S12). Using Eq. **7**, we can calculate the morphogen concentration a distance $\epsilon\lambda$ away from a boundary of curvature κ to get (*SI Appendix* has the derivation assuming arbitrary ϵ) to the leading order in $\kappa\lambda$:

$$\frac{\psi_{\epsilon,\kappa}}{\psi_{bulk}} = \frac{1 + \epsilon - \kappa\lambda}{2}. \qquad [8]$$

This expression gives 1/2 when $\kappa\lambda = \epsilon = 0$, which corresponds to a sphere cut in half by a plane. Cells stop dividing when the concentration drops below a certain threshold, written as $\psi_{\epsilon,\kappa} < f\, \psi_{bulk}$, for some choice of fraction $0 < f < 1$. Since $\epsilon\lambda$ is the thickness of the layer of cells that stop cell division and denoting the cell division time as T_c, the velocity of the cross-section can be written as $\mathbf{v} = -(\epsilon\lambda/T_c)\mathbf{n}$ (*SI Appendix* has more details). After solving the condition $\psi_{\epsilon,\kappa} = f\, \psi_{bulk}$ for ϵ in Eq. **8**, we get the modified mean curvature flow with coefficients

$$a = (2f - 1)\frac{\lambda}{T_c} > 0, \quad b = \frac{\lambda^2}{T_c} > 0. \qquad [9]$$

Note that both coefficients are generically expected to be positive provided that cell division stops below a concentration threshold and cells near straight boundary regions ($\kappa = 0$) are below this threshold ($2f > 1$).

From previous measurements on developing zebra finch beaks (9) (*SI Appendix*, Fig. S11), we calculate the extrusion rate to be $U \approx 29\ \mu$m/h, which is within an order of magnitude from the estimate $U \sim W_c/T_c$, where $W_c \sim 10 - 100\ \mu$m is the cell width (41) and $T_c \sim 1 - 24$h is the time between cell divisions (42). In addition, we find experimentally that $b \approx 22\ \mu\text{m}^2$/h (*SI Appendix*, Fig. S11), which is within an order of magnitude of the value obtained from Eq. **9** using $\lambda \sim 50 - 100\ \mu$m (43). Lastly, we estimate $b/(UW) \sim 0.01$, where $W \sim 80]$, μm is taken as the growth zone size 100 h before it reaches the tip (*SI Appendix*, Fig. S11), which is comparable with the values $b/(UW) \sim 0.05$ in Fig. 5. Since this is a dimensionless quantity, we expect it to stay relatively constant beyond this stage as the beak size increases without considerable change in shape (9, 44). Thus, the cell-level growth model leads to the tissue-level model, which was fitted to the beak shapes, and both give consistent estimates of the growth parameters.

Circular Cross-Sections and Developmental Constraints. The parameter b can be estimated by comparing the solution of the growth equations $R(\tau)$ with the width given by Eq. **4** and recalling that $W(\tau) = 2R(\tau)$. Near the tip ($tU/L = \tau \to 1$), we have

$$W(\tau) \approx W \sqrt{\frac{4\ (1 + \tilde{\kappa}_x)}{4 + \tilde{S}}}\ \sqrt{(1 - \tau)}, \quad R(\tau) \approx \sqrt{\frac{2bL}{U}}\sqrt{(1 - \tau)}.$$
$$\implies \frac{b}{UW} = \frac{(1 + \tilde{\kappa}_x)}{4 + \tilde{S}}\frac{W}{2L}, \qquad [10]$$

where the first equality follows from Eq. **4** and the second follows from the growth law applied to circular cross-sections (*SI Appendix*).

We assume that $a > 0, b > 0$. If this was not the case, then we would have a finite width fixed point in the dynamics. For a given value of b, the largest possible length L happens when $a = 0$ (since a positive value of a leads to lower lengths via faster width decay). When $a = 0$, we have $\dot{R} = -b/R \implies R(t) = \sqrt{2b(L/U - t)}$. From the initial conditions, we get $R(0) = W/2 = \sqrt{2bL/U} \implies b/U = W^2/8L$. This is a constraint because any larger value of L would require negative values of a. Therefore, we get the prediction $b/(WU) < W/8L$, which is satisfied by our samples (Fig. 5). Using the equation above for b in terms of other morphological parameters, we get $4\tilde{\kappa}_x \leq \tilde{S}$.

Data Availability. Raw mesh data and code used to generate results have been deposited in Harvard Dataverse (https://doi.org/10.7910/DVN/IHODX1) (16). All other data are included in the manuscript and/or supporting information.

ACKNOWLEDGMENTS. This work was supported in part by NSF Grants DMS-2002103 (to G.P.T.C.) and NSF-1257122 (to A.A.), Harvard Quantitative Biology Initiative and NSF–Simons Center for Mathematical and Statistical Analysis of Biology at Harvard Award 1764269 (to G.P.T.C. and L.M.), the Simons Foundation (L.M.), and the Henri Seydoux Fund (L.M.).

1. S. Lamichhaney *et al.*, A beak size locus in Darwin's finches facilitated character displacement during a drought. *Science* **352**, 470–474 (2016).
2. P. R. Grant, B. R. Grant, Adaptive radiation of Darwin's finches: Recent data help explain how this famous group of Galapagos birds evolved, although gaps in our understanding remain. *Am. Sci.* **90**, 130–139 (2002).
3. A. M. Reaney, Y. Bouchenak-Khelladi, J. A. Tobias, A. Abzhanov, Ecological and morphological determinants of evolutionary diversification in Darwin's finches and their relatives. *Ecol. Evol.* **10**, 14020–14032 (2020).
4. P. R. Grant, B. R. Grant, Evolution of character displacement in Darwin's finches. *Science* **313**, 224–226 (2006).
5. M. Sakamoto, M. Ruta, C. Venditti, Extreme and rapid bursts of functional adaptations shape bite force in amniotes. *Proc. Biol. Sci.* **286**, 20181932 (2019).
6. A. Abzhanov, M. Protas, B. R. Grant, P. R. Grant, C. J. Tabin, Bmp4 and morphological variation of beaks in Darwin's finches. *Science* **305**, 1462–1465 (2004).
7. A. Abzhanov *et al.*, The calmodulin pathway and evolution of elongated beak morphology in Darwin's finches. *Nature* **442**, 563–567 (2006).
8. R. Mallarino *et al.*, Two developmental modules establish 3D beak-shape variation in Darwin's finches. *Proc. Natl. Acad. Sci. U.S.A.* **108**, 4057–4062 (2011).
9. J. A. Fritz *et al.*, Shared developmental programme strongly constrains beak shape diversity in songbirds. *Nat. Commun.* **5**, 3700 (2014).
10. D. J. Foster, J. Podos, A. P. Hendry, A geometric morphometric appraisal of beak shape in Darwin's finches. *J. Evol. Biol.* **21**, 263–275 (2008).
11. M. Tokita, W. Yano, H. F. James, A. Abzhanov, Cranial shape evolution in adaptive radiations of birds: Comparative morphometrics of Darwin's finches and Hawaiian honeycreepers. *Philos. Trans. R. Soc. Lond. B Biol. Sci.* **372**, 20150481 (2017).
12. A. Herrel *et al.*, Adaptation and function of the bills of Darwin's finches: Divergence by feeding type and sex. *Emu* **110**, 39–47 (2010).
13. J. Soons *et al.*, Mechanical stress, fracture risk and beak evolution in Darwin's ground finches (Geospiza). *Philos. Trans. R. Soc. Lond. B Biol. Sci.* **365**, 1093–1098 (2010).
14. P. R. Grant, The feeding of Darwin's finches on *Tribulus cistoides* (L.) seeds. *Anim. Behav.* **29**, 785–793 (1981).
15. O. Campàs, R. Mallarino, A. Herrel, A. Abzhanov, M. P. Brenner, Scaling and shear transformations capture beak shape variation in Darwin's finches. *Proc. Natl. Acad. Sci. U.S.A.* **107**, 3356–3360 (2010).
16. S. al-Mosleh, G. P. T. Choi, A. Abzhanov, L. Mahadevan, Code and Data. Harvard Dataverse. https://doi.org/10.7910/DVN/IHODX1. Deposited 8 October 2021.

17. J. Podos, Correlated evolution of morphology and vocal signal structure in Darwin's finches. *Nature* **409**, 185–188 (2001).
18. G. Navalón, J. A. Bright, J. Marugán-Lobón, E. J. Rayfield, The evolutionary relationship among beak shape, mechanical advantage, and feeding ecology in modern birds. *Evolution* **73**, 422–435 (2019).
19. G. Navalón, J. Marugán-Lobón, J. A. Bright, C. R. Cooney, E. J. Rayfield, The consequences of craniofacial integration for the adaptive radiations of Darwin's finches and Hawaiian honeycreepers. *Nat. Ecol. Evol.* **4**, 270–278 (2020).
20. P. T. Boag, P. R. Grant, Intense natural selection in a population of Darwin's finches (Geospizinae) in the Galapagos. *Science* **214**, 82–85 (1981).
21. J. Soons *et al.*, Is beak morphology in Darwin's finches tuned to loading demands? *PLoS One* **10**, e0129479 (2015).
22. A. M. Olsen, Feeding ecology is the primary driver of beak shape diversification in waterfowl. *Funct. Ecol.* **31**, 1985–1995 (2017).
23. A. Herrel, J. Podos, S. K. Huber, A. P. Hendry, Evolution of bite force in Darwin's finches: A key role for head width. *J. Evol. Biol.* **18**, 669–675 (2005).
24. M. A. van der Meij, R. G. Bout, The relationship between shape of the skull and bite force in finches. *J. Exp. Biol.* **211**, 1668–1680 (2008).
25. L. M. Witmer, K. D. Rose, Biomechanics of the jaw apparatus of the gigantic Eocene bird Diatryma: Implications for diet and mode of life. *Paleobiology* **17**, 95–120 (1991).
26. J. J. Uicker, G. R. Pennock, J. E. Shigley, J. M. Mccarthy, *Theory of Machines and Mechanisms* (Oxford University Press, New York, NY, 2003), **vol. 3**.
27. J. R. Murray, C. W. Varian-Ramos, Z. S. Welch, M. S. Saha, Embryological staging of the Zebra Finch, *Taeniopygia guttata*. *J. Morphol.* **274**, 1090–1110 (2013).
28. J. A. Helms, R. A. Schneider, Cranial skeletal biology. *Nature* **423**, 326–331 (2003).
29. J. M. Richman, S. H. Lee, About face: Signals and genes controlling jaw patterning and identity in vertebrates. *BioEssays* **25**, 554–568 (2003).
30. P. Wu, T. X. Jiang, J. Y. Shen, R. B. Widelitz, C. M. Chuong, Morphoregulation of avian beaks: Comparative mapping of growth zone activities and morphological evolution. *Dev. Dyn.* **235**, 1400–1412 (2006).
31. J. P. Keener, A geometrical theory for spiral waves in excitable media. *SIAM J. Appl. Math.* **46**, 1039–1056 (1986).
32. J. J. Tyson, J. P. Keener, Singular perturbation theory of traveling waves in excitable media (a review). *Physica D* **32**, 327–361 (1988).
33. J. Rubinstein, P. Sternberg, J. B. Keller, Fast reaction, slow diffusion, and curve shortening. *SIAM J. Appl. Math.* **49**, 116–133 (1989).
34. P. Grindrod, M. A. Lewis, J. D. Murray, A geometrical approach to wave-type solutions of excitable reaction-diffusion systems. *Proc. R. Soc. A* **433**, 151–164 (1991).
35. L. Rayleigh, The ultimate shape of pebbles, natural and artificial. *Proc. R. Soc. Lond. A Math. Phys. Sci.* **181**, 107–118 (1942).
36. W. W. Mullins, Two-dimensional motion of idealized grain boundaries. *J. Appl. Phys.* **27**, 900–904 (1956).
37. M. A. Grayson, The heat equation shrinks embedded plane curves to round points. *J. Differ. Geom.* **26**, 285–314 (1987).
38. G. Perelman, Finite extinction time for the solutions to the Ricci flow on certain three-manifolds. arXiv [Preprint] (2003). https://arxiv.org/abs/math/0307245 (Accessed 8 October 2021).
39. A. Goswami, Phenome10K: A free online repository for 3-D scans of biological and palaeontological specimens (2015). https://www.phenome10k.org/. Accessed 16 May 2020.
40. T. Uller, A. P. Moczek, R. A. Watson, P. M. Brakefield, K. N. Laland, Developmental bias and evolution: A regulatory network perspective. *Genetics* **209**, 949–966 (2018).
41. D. A. Guertin, D. M. Sabatini, *Cell Size Control* (American Cancer Society, 2006).
42. G. M. Cooper, R. E. Hausman, *The Cell: A Molecular Approach* (ASM Press, Washington, DC, 2007), **vol. 4**, pp. 649–656.
43. O. Wartlick, A. Kicheva, M. González-Gaitán, Morphogen gradient formation. *Cold Spring Harb. Perspect. Biol.* **1**, a001255 (2009).
44. A. Genbrugge *et al.*, Ontogeny of the cranial skeleton in a Darwin's finch (Geospiza fortis). *J. Anat.* **219**, 115–131 (2011).